Two-Dimensional Hybrid Organic-Inorganic Perovskite Nanosheets for Gb/s Visible-Light Communication

Yue Wang, *Graduate Student Member, IEEE*, Hong Wang,

Omar Alkhazragi, *Graduate Student Member, IEEE*, Zyad O. F. Mohammed, Luis Gutiérrez-Arzaluz,

Chun Hong Kang, *Member, IEEE*, Tien Khee Ng, *Senior Member, IEEE*,

and Boon S. Ooi, *Senior Member, IEEE*

Abstract—With the rapid development of solid-state lighting and the congestion of radio-frequency communication data traffic, visible-light communication (VLC) has emerged as a versatile technology for simultaneous illumination and communication. However, the conventional color-converting phosphors integrated with light-emitting diodes (LEDs), or laser diodes (LDs) usually have limited optical modulation bandwidth due to the long carrier recombination lifetime, which is not suitable for high-speed multiple-wavelength data transfer based on phosphor-conversion VLC systems. Herein, we demonstrate a hybrid organic-inorganic perovskite nanosheets (NSs), i.e., $(C_8N_9NH_3)_2PbI_4$ (PEPI), passivated by polymer, as a fast-acting color-converting phosphor for VLC. Compared to the PEPI micro-plates (μPs), the NSs exhibit a stronger excitonic effect with a shorter fluorescence lifetime of 877 ± 4.7 ps, leading to a broad -3-dB bandwidth of 192.8 MHz. Given the large bandwidth, a net data rate of 0.93 Gb/s was achieved based on an orthogonal frequency-division multiplexing (OFDM) modulation scheme. These investigations verified the feasibility of using two-dimensional hybrid organic-inorganic perovskite materials as a promising phosphor for future multi-Gb/s color-pure wavelength-division multiplexing systems.

Index Terms—Fast-acting phosphors, optical wireless communication, 2D hybrid organic-inorganic perovskite.

I. INTRODUCTION

VISIBLE-LIGHT communication (VLC), as a subset of optical wireless communication, is an emerging technology for data transmission by modulating visible light at

Yue Wang, Omar Alkhazragi, Zyad O. F. Mohammed, Chun Hong Kang, Tien Khee Ng, and Boon S. Ooi are with the Photonics Laboratory, Division of Computer, Electrical, and Mathematical Sciences and Engineering, King Abdullah University of Science and Technology, Thuwal 23955, Saudi Arabia (e-mail: boon.ooi@kaust.edu.sa).

Hong Wang and Luis Gutiérrez-Arzaluz are with the Advanced Membrane and Porous Material Center and the KAUST Catalysis Center, Division of Physical Science and Engineering, King Abdullah University of Science and Technology, Thuwal 23955, Saudi Arabia.

wavelengths from 400 nm to 700 nm. Possessing such a wide unlicensed spectrum, VLC can significantly extend the usable bandwidth not feasible with radio frequency (RF) communication alone. Light sources (i.e., light-emitting diodes (LEDs), laser diodes (LDs), or superluminescent diodes (SLDs)) and photodetectors (PDs) are recently being developed rapidly for light-fidelity, wireless communication links for the internet of things, vehicle-to-vehicle communication, and underwater wireless optical communication [1], [2].

Phosphor, albeit an essential component, typically affects the overall VLC performance. In addition, phosphor is used in white-light illumination to achieve high color rendering index when excited using a violet/blue LD [3], [4], and increasingly investigated for VLC and photodetection. By designing a scenario-specific color-converting phosphor, such as by selecting materials or by shaping the form factor, one could shift the re-emitted wavelength to closely match the higher responsivity of the off-the-shelf PD and/or circumvent the étendue limit for wider field-of-view high-speed photodetection [5], [6]. To date, the conventional phosphors still suffer from a long fluorescent lifetime, which significantly limits the modulation bandwidth of VLC systems. To this end, researchers continue to explore different materials, including organic-based materials, metal-organic frameworks, perovskites of different dimensionalities (i.e., quantum dots (QDs), nanowires, nanocrystals (NCs), and bulk single crystal (SC)), or design nanopatterned metamaterials to achieve a color-converting phosphor with a wide modulation bandwidth, high photoluminescence quantum yield (PLQY), high stability, non-toxicity, and ease of synthesis or fabrication [7]–[11].

Recently, two-dimensional (2D) hybrid organic-inorganic halide-perovskites have drawn increasing research attention due to their unique features compared to the bulk structure. For halide-based perovskites, a 2D layered structure is commonly arranged based on the Ruddlesden-Popper phase with a general chemical formula of $L_2[ABX_3]_{n-1}BX_4$, where L is a large organic cation (i.e., phenylethylammonium (PEA$^+$) and butylammonium (BA$^+$)), A is a monovalent cation (i.e., methylammonium (MA$^+$) and formamidium (FA$^+$)), B is a divalent metal cation (i.e., Pb^{2+}, Sn^{2+}, Cu^{2+}, and Mn^{2+}), X is a halide anion (i.e., Cl$^-$, Br$^-$, and I$^-$), and n is the

TABLE I
COMPARISON OF PL LIFETIME AND MODULATION BANDWIDTH OF
DIFFERENT COLOR-CONVERTING PHOSPHORS

Material	PL Lifetime τ	$f_{\text{-3-dB}}$ (MHz)	Ref.
Ir-Lpt-CN	17 μs	26.3	[7]
RhB@Al-DBA	5.3 ns	3.6	[8]
$Cs_3Cu_2I_5$ / $CsCu_2I_3$ SC	1 μs / 52.99 ns	10.1	[9]
PbS QDs	6.4 μs	< 1	[16]
$CsPbBr_3$ NCs	4.5 ± 0.1 ns	70.92	[5]
$CsPbBr_{1.8}I_{1.2}$ QDs	43.74 ns	73	[17]
$CsPbBr_3@ZrO_2$ NCs	10s ns	2.75	[18]
$(PEA)_2PbI_4$ NSs	**877.4 ± 4.7 ps**	**192.8**	**This work**

* The data shown in this table are closely matched with $f_{\text{-3-dB}} \leq \frac{1}{2\pi\tau}$.

* In these works, the bandwidths were measured with the excitation light fully filtered at the receiver end unlike filter-free white-light communication [19].

number of inorganic $[BX_6]^{4-}$ octahedral layers between the two layers of the organic chain. When $n \leq 3$, it can be defined as a 2D nanosheet, which exhibits higher excitonic effects caused by higher quantum confinement. Furthermore, because of its low trap-state density, strong PL, and facile synthesis, this material shows great potential for optical devices, such as organic-based LEDs, optical modulators, PDs, and photovoltaic devices [12]–[14]. Also, by adjusting the halide anions, metal cations, or layer thickness, the emission of 2D halide perovskites can be tuned covering the entire visible spectrum [15], which could fulfill high-speed color-pure wavelength-division multiplexing (WDM) by using a single source with multiple phosphors emitting light at different wavelengths.

Herein, we used phenylethylammonium lead iodide, $(PEA)_2PbI_4$ with PEA = $C_8N_9NH_3$ (PEPI henceforth), to form 2D nanosheets (NSs) and micro-plates (μPs), which are differed by dimensions. We then encapsulated the perovskite in the polymethyl methacrylate (PMMA). The resultant thin film can convert a 405-nm laser beam into ~530-nm green light in a VLC link. Compared with PEPI μPs, the shorter lifetime of PEPI NSs (~877 ps) contributes to a wider −3-dB bandwidth of 192.8 MHz. A high gross data rate of 1.1 Gb/s was achieved by using a direct-current-biased optical orthogonal frequency-division multiplexing (DCO-OFDM) scheme. We demonstrated, for the first time, the use of PEPI NSs as a fast-acting wavelength-converting phosphor for VLC with a higher data rate as compared to other materials previously reported (Table I).

II. MATERIAL CHARACTERIZATION

The PEPI NSs and μPs were synthesized using the same methods as Refs. [20] and [21], respectively. Scanning electron microscopy (SEM, Zeiss Merlin) was used to image the PEPI NSs on silicon and the PEPI μPs powder (see insets in Fig. 1). For PEPI μPs, the SEM image shows a bulk-like aggregation, and the dimension of an individual plate can be larger than 5 μm. While the NSs are more dispersed at the same scale as μPs. The average area of multi-layer NSs is approximately 0.09 μm^2 with a thickness larger than 100 nm. For NSs with fewer layers, the thickness is less than 7 nm (i.e.,
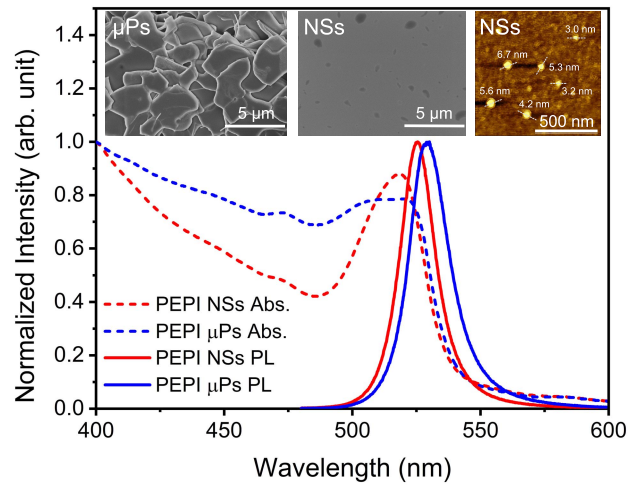

Fig. 1. Normalized absorbance and PL spectra of PEPI NSs and μPs in PMMA. The insets show the SEM images of PEPI μPs (left), PEPI NSs (middle), and AFM image of PEPI NSs (right).

≤ 3 layers) as verified with atomic force microscopy (AFM, Bruker Dimension Icon) of a 1×1 μm^2 area (see inset in Fig. 1). To ensure the durability and flexibility of the proposed material for the subsequent experiments, the synthesized PEPI powder (1 wt%) was uniformly mixed with PMMA in a chloroform solution, which was then dropped in a glass vial subsequently. A free-standing thin film with a thickness of ~300 μm was obtained after the solvent evaporated overnight.

The PL spectra of NSs and μPs in PMMA were measured under 473-nm excitation using a PL/Raman measuring instrument (WITec Apyron). Both samples exhibited sharp PL spectra with peak emission wavelengths of ~525 nm for NSs and ~529 nm for μPs in Fig. 1. The full width at half maximum (FWHM) is approximately 14.7 nm and 16.3 nm for NSs and μPs, respectively. The PL peak showed a slight red shift from NSs to μPs, indicative of the change in bandgap depending on the dimensionality. It was reported that increasing the number of layers weakens the quantum confinement and shrinks the bandgap, causing the redshift and the wider FWHM [22], [23]. This thickness-dependent property can also be verified by absorbance measurement in spectrophotometry (Shimadzu, UV-3600). Compared to the μPs, the NSs show a stronger excitonic absorption at 518 nm, implying a higher exciton binding energy arising from better quantum confinement and dielectric confinement introduced by the smaller thickness of the NSs [24]. The PLQY of NSs was measured to be 27% using a fluorospectrometer (Horiba FluoroMax-4).

To test the small-signal frequency response of the proposed material, a communication link was established with a 405-nm violet LD (SaNoor Technologies, SNLDP03), an integrating sphere to place the sample, and a silicon-based avalanche photodetector (APD, Thorlabs, APD430A2/M) (see Fig. 2). The laser beam was coupled into the integrating sphere and focused on the sample. The fluorescence of the sample was collected by two aspheric condenser lenses and a $100\times$ objective lens. A 450-nm long-pass (LP) filter (Thorlabs, FELH0450) was used to remove the laser light. For back-end electronics, a bias-tee (Mini-Circuits, ZFBT-4R2GW-FT+) was used to combine
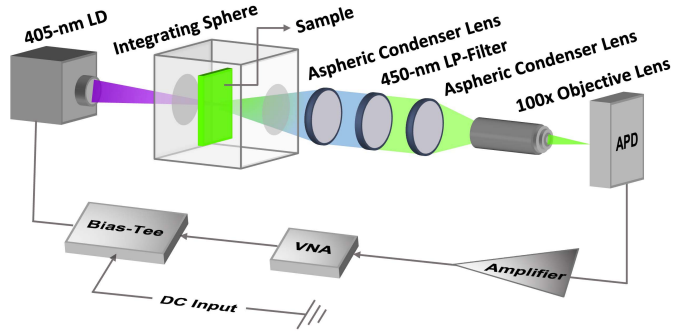
Fig. 2.   Schematic diagram of the small-signal frequency response setup.

Fig. 3.   (a) Normalized frequency responses with PEPI NSs and μPs in PMMA by fully filtering the laser light. The inset shows the normalized frequency responses without an LP filter. (b) TCSPC measurement for PEPI NSs and μPs in PMMA with the corresponding fitting curves.

the DC bias of 4.6 V with the alternating current (AC) signal to drive the LD. A 25-dB amplifier (Mini-Circuits, ZHL-6A+) was used to amplify the output signal from the APD. A vector network analyzer (VNA) (Agilent Technologies, E5061B) was pre-calibrated and utilized to generate the modulation signal from 300 kHz to 400 MHz. The light-source/sample and sample/APD distances are 0.2 m for the proof-of-concept setup.

The normalized frequency response spectra of both NSs and μPs are shown in Fig. 3(a). To investigate the capability of 2D PEPI for high-speed color-pure WDM, -3-dB bandwidths of 192.8 MHz with the NSs and 104.3 MHz with the μPs were achieved when the light from the transmitter was filtered by the 450-nm LP filter. Moreover, the gradual decrease after the -3-dB response offers a usable bandwidth up to 395 MHz for NSs using OFDM with adaptive bit and power loading. To ensure that there was no contribution to the overall bandwidth from the excitation source, we removed the LP filter and obtained a 592-MHz bandwidth with the same samples (see inset of Fig. 3(a)), which was remarkably broadened by the transmitter with 632-MHz bandwidth. As the main factor that affects the modulation bandwidth, the PL lifetimes of both PEPI NSs and μPs in PMMA were investigated using the time-correlated single-photon counting (TCSPC) technique. Under the excitation of a 405-nm pulsed LD (Horiba, Delta Diode), and detecting the PL with an APD (PicoQuant), the PL lifetime was extracted by fitting the PL decay trace. As shown in Fig. 3(b), the average lifetimes fitted using triexponential decay functions for PEPI NSs is 877.4 $\pm$ 4.7 ps and the lifetime of PEPI μPs is 2556 $\pm$ 5.8 ps, indicating the material which has a shorter PL lifetime tends to have wider -3-dB bandwidth.

III. VLC Performance

We tested the performance of the system using DCO-OFDM as the communication scheme and the same optics shown in Fig. 2, but with different electronics described below. In this test, the signal was sent to the LD using an arbitrary waveform generator (AWG, Tektronix, AWG70002A). Given the limited signal peak-to-peak amplitude from the AWG (≤ 0.5 V), the signal was sent through an amplifier (Mini-Circuits, ZHL-2-8-S+) before being fed to the LD through the bias tee. An identical amplifier was used on the receiver side with a variable attenuator to control the amplitude of the signal to be recorded by the oscilloscope (Tektronix,
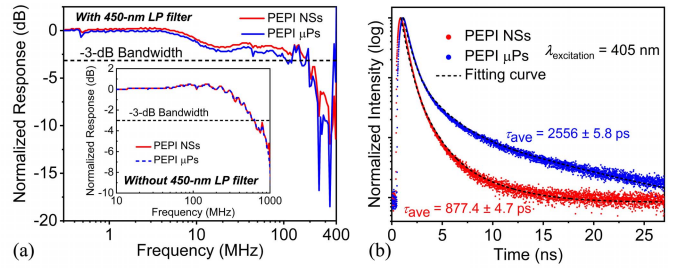
MDO3104) at a sampling rate of 2500 MSamples/s for offline processing (see Ref. [25]).

The sampling rate of the AWG, f_{AWG}, was set to 800 MSamples/s and the size of the inverse fast Fourier transform (IFFT), N_{FFT}, was set to 1024, meaning each subcarrier has a bandwidth of around 0.8 MHz. Data was loaded onto subcarriers 6–505, corresponding to the frequency range 4–395 MHz. In other words, the number of subcarriers used, N_{SC}, was 500. The reason for avoiding the low-frequency range is to avoid the low response of the used electronics at low frequencies. In all tests, the modulated signal was a $2^{16}-1$ pseudorandom binary sequence (PRBS).

To estimate the signal-to-noise ratio (SNR) for each subcarrier, a uniform 4-quadrature-amplitude-modulation (4-QAM) signal consisting of 150 OFDM symbols along with their respective cyclic prefixes was sent through the system and the SNR is estimated (see Fig. 4(a)) using the error vector magnitude. The size of each cyclic prefix $N_{\text{CP}} = 10$, which was used to minimize inter-symbol interference (ISI) and simplify post-equalization. After calculating the channel capacity, the appropriate bit/power loading schemes were implemented. The relatively low SNR of the first few subcarriers is caused by the low gain region of the electronic amplifiers. The maximum constellation size was 32-QAM. Fig. 4(b) insets show the constellation diagrams formed by superimposing constellations from all subcarriers loaded with the same QAM order.

The gross data rate of 1.1 Gb/s was achieved with a bit error ratio ($BER = 3.7 \times 10^{-3}$) below 7%-overhead forward error correction (FEC) BER limit (3.8×10^{-3}) using adaptive bit and power loading. The calculation can be expressed as follows:

$$\text{Gross data rate} = \frac{f_{\text{AWG}}}{N_{\text{FFT}} + N_{\text{CP}}} \sum_{k=1}^{N_{SC}} \log_2 (M_k)$$

where $M_k = 2^b$ is the QAM order of the kth subcarrier (disregarding the five empty subcarriers inserted at the beginning) and b is the number of bits allocated correspondingly. After accounting for the 8% training symbols used for synchronization and channel estimation used for single-tap post-equalization, the data rate is 1.0 Gb/s. Therefore, the overall net data rate assuming a 7% overhead used for FEC is 0.93 Gb/s. This high data rate is probably attributed to the short PL lifetime of the NSs as well as the spectral efficiency
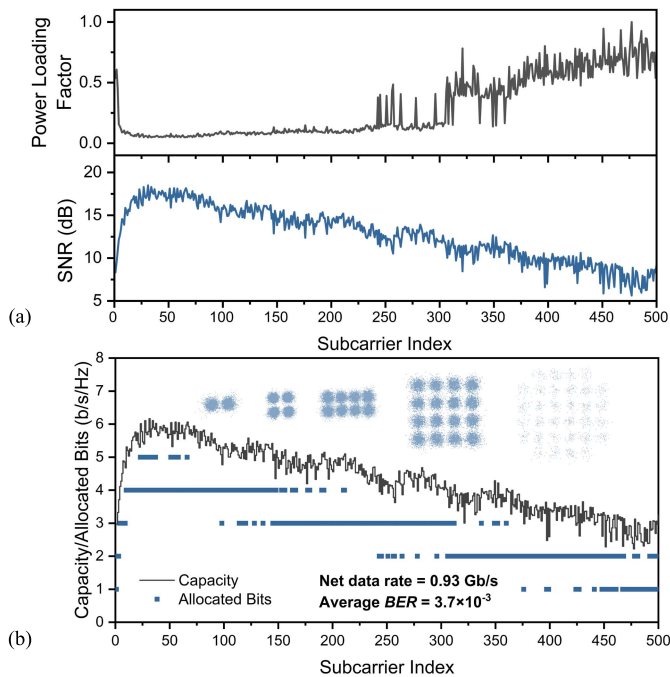
Fig. 4. DCO-OFDM implementation for PEPI NSs in PMMA. (a) Power loading factor and SNR of each subcarrier. (b) Channel capacity and allocated number of bits for each subcarrier with the constellation diagrams (insets).

of the modulation scheme implemented, which was adaptively designed to match the performance of the NSs. When the same communication technique was applied for the μPs, the usable bandwidth was only 3.2–320.6 MHz, which is limited by the longer PL lifetime, and the net data rate was 0.66 Gb/s with an average *BER* of 3.6×10^{-3}.

IV. CONCLUSION

We have investigated a 2D hybrid organic-inorganic perovskite, PEPI, in two different morphologies (NSs and μPs) as fast-acting wavelength-converting luminescent phosphors for the Gb/s VLC link. By taking advantage of the strong PL, narrow linewidth (14.7 nm), large exciton binding energy, and short PL lifetime (877.4 ± 4.7 ps) provided by NSs, a 192.8 MHz -3-dB bandwidth and a 0.93 Gb/s net data rate were realized using DCO-OFDM with optimized bit and power loading, solely attributed to the converted light. This study paved the way forward for the integration of 2D hybrid organic-inorganic perovskite-based luminescent material in high-speed optical devices and optical wireless communication systems.

REFERENCES

[1] L. U. Khan, "Visible light communication: Applications, architecture, standardization and research challenges," *Digit. Commun. Netw.*, vol. 3, no. 2, pp. 78–88, May 2017.

[2] H. M. Oubei *et al.*, "4.8 Gbit/s 16-QAM-OFDM transmission based on compact 450-nm laser for underwater wireless optical communication," *Opt. Exp.*, vol. 23, no. 18, pp. 23302–23309, Sep. 2015.

[3] C.-Y. Su *et al.*, "Color-converting violet laser diode with an ultrafast BEHP-PPV + MEH-PPV polymer blend for high-speed white lighting data link," *ACS Appl. Electron. Mater.*, vol. 2, no. 9, pp. 3017–3027, Sep. 2020.

[4] Z. Wang *et al.*, "Encapsulation-enabled perovskite–PMMA films combining a micro-LED for high-speed white-light communication," *ACS Appl. Mater. Interface*, vol. 13, no. 45, pp. 54143–54151, Nov. 2021.

[5] C. H. Kang *et al.*, "High-speed colour-converting photodetector with all-inorganic CsPbBr$_3$ perovskite nanocrystals for ultraviolet light communication," *Light, Sci. Appl.*, vol. 8, no. 1, pp. 1–12, Oct. 2019.

[6] P. P. Manousiadis *et al.*, "Wide field-of-view fluorescent antenna for visible light communications beyond the étendue limit," *Optica*, vol. 3, no. 7, pp. 702–706, Jun. 2016.

[7] W. Li *et al.*, "Efficient yellow phosphorescent [3+2+1] Ir (III) complex for warm white lighting and visible light communication," *Mater. Today Energy*, vol. 23, Jan. 2022, Art. no. 100892.

[8] Z. Wang *et al.*, "Warm-white-light-emitting diode based on a dye-loaded metal–organic framework for fast white-light communication," *ACS Appl. Mater. Interface*, vol. 9, no. 40, pp. 35253–35259, Oct. 2017.

[9] B. Wang *et al.*, "Pressure-assisted cooling to grow ultra-stable Cs$_3$Cu$_2$I$_5$ and CsCu$_2$I$_3$ single crystals for solid-state lighting and visible light communication," *EcoMat*, vol. 4, no. 2, Jan. 2022, Art. no. e12184.

[10] X. Yang *et al.*, "Enhancing communication bandwidths of organic color converters using nanopatterned hyperbolic metamaterials," *J. Lightw. Technol.*, vol. 36, no. 10, pp. 1862–1867, May 15, 2018.

[11] J.-X. Wang *et al.*, "Metal–organic frameworks in mixed-matrix membranes for high-speed visible-light communication," *J. Amer. Chem. Soc.*, vol. 144, no. 15, pp. 6813–6820, Apr. 2022.

[12] K. Wang, J. Y. Park, and L. Dou, "Two-dimensional halide perovskite quantum-well emitters: A critical review," *EcoMat*, vol. 3, no. 3, Jun. 2021, Art. no. e12104.

[13] G. Grinblat *et al.*, "Ultrafast all-optical modulation in 2D hybrid perovskites," *ACS Nano*, vol. 13, no. 8, pp. 9504–9510, Aug. 2019.

[14] Y. Tu *et al.*, "Ultrathin single-crystalline 2D perovskite photoconductor for high-performance narrowband and wide linear dynamic range photodetection," *Small*, vol. 16, no. 52, Dec. 2020, Art. no. 2005626.

[15] M. C. Weidman, M. Seitz, S. D. Stranks, and W. A. Tisdale, "Highly tunable colloidal perovskite nanoplatelets through variable cation, metal, and halide composition," *ACS Nano*, vol. 10, no. 8, pp. 7830–7839, Aug. 2016.

[16] A. Tankimanova *et al.*, "Colloidal PbS quantum dots for visible-to-near-infrared optical Internet of Things," *IEEE Photon. J.*, vol. 13, no. 2, pp. 1–11, Apr. 2021.

[17] S. Mei *et al.*, "High-bandwidth white-light system combining a micro-LED with perovskite quantum dots for visible light communication," *ACS Appl. Mater. Interfaces*, vol. 10, no. 6, pp. 5641–5648, Feb. 2018, doi: 10.1021/acsami.7b17810.

[18] Q. Mo, C. Chen, W. Cai, S. Zhao, D. Yan, and Z. Zang, "Room temperature synthesis of stable zirconia-coated CsPbBr$_3$ nanocrystals for white light-emitting diodes and visible light communication," *Laser Photon. Rev.*, vol. 15, no. 10, Oct. 2021, Art. no. 2100278.

[19] A. Ali *et al.*, "Blue-laser-diode–based high CRI lighting and high-speed visible light communication using narrowband green-/red-emitting composite phosphor film," *Appl. Opt.*, vol. 59, no. 17, pp. 5197–5204, Jun. 2020.

[20] S. Yang *et al.*, "Ultrathin two-dimensional organic-inorganic hybrid perovskite nanosheets with bright, tunable photoluminescence and high stability," *Angew. Chem.*, vol. 129, no. 15, pp. 4316–4319, Apr. 2017.

[21] H. Wang *et al.*, "Mechanistic understanding of efficient photocatalytic H$_2$ evolution on two-dimensional layered lead iodide hybrid perovskites," *Angew. Chem.*, vol. 133, no. 13, pp. 7452–7457, Mar. 2021.

[22] Z. Guo, X. Wu, T. Zhu, X. Zhu, and L. Huang, "Electron–phonon scattering in atomically thin 2D perovskites," *ACS Nano*, vol. 10, no. 11, pp. 9992–9998, Nov. 2016.

[23] Q. Zhang, L. Chu, F. Zhou, W. Ji, and G. Eda, "Excitonic properties of chemically synthesized 2D organic-inorganic hybrid perovskite nanosheets," *Adv. Mater.*, vol. 30, no. 18, May 2018, Art. no. 1704055.

[24] G. Walters *et al.*, "The quantum-confined stark effect in layered hybrid perovskites mediated by orientational polarizability of confined dipoles," *Nature Commun.*, vol. 9, no. 1, pp. 1–11, Oct. 2018.

[25] C. H. Kang *et al.*, "All-inorganic halide-perovskite polymer-fiber-photodetector for high-speed optical wireless communication," *Opt. Exp.*, vol. 30, no. 6, p. 9823, Mar. 2022.